Open-Circuit Voltage in Organic Solar Cells: The Impacts of Donor Semicrystallinity and Coexistence of Multiple Interfacial Charge-Transfer Bands

*Guy O. Ngongang Ndjawa, Kenneth R. Graham, Sonya Mollinger, Di M. Wu, David Hanifi, Rohit Prasanna, Bradley D. Rose, Sukumar Dey, Liyang Yu, Jean-Luc Brédas, Michael D. McGehee, Alberto Salleo, and Aram Amassian**

In organic solar cells (OSCs), the energy of the charge-transfer (CT) complexes at the donor–acceptor interface, E_{CT}, determines the maximum open-circuit voltage (V_{OC}). The coexistence of phases with different degrees of order in the donor or the acceptor, as in blends of semi-crystalline donors and fullerenes in bulk heterojunction layers, influences the distribution of CT states and the V_{OC} enormously. Yet, the question of how structural heterogeneities alter CT states and the V_{OC} is seldom addressed systematically. In this work, we combine experimental measurements of vacuum-deposited rubrene/C_{60} bilayer OSCs, with varying microstructure and texture, with density functional theory calculations to determine how relative molecular orientations and extents of structural order influence E_{CT} and V_{OC}. We find that varying the microstructure of rubrene gives rise to CT bands with varying energies. The CT band that originates from crystalline rubrene lies up to ≈0.4 eV lower in energy compared to the one that arises from amorphous rubrene. These low-lying CT states contribute strongly to V_{OC} losses and result mainly from hole delocalization in aggregated rubrene. This work points to the importance of realizing interfacial structural control that prevents the formation of low E_{CT} configurations and maximizes V_{OC}.

1. Introduction

For organic solar cells to efficiently convert absorbed photons into electricity, it is essential to minimize recombination and energetic losses at the charge dissociating interfaces.[1–7] In the vast majority of state-of-the-art organic solar cells, this dissociating interface is the junction between electron donor (D) and acceptor (A) phases. Here, frontier molecules of D and A are coupled electronically, forming a molecular complex on which excited states reside before they either dissociate into free carriers or recombine to the ground state. These intermolecular excited states are referred to as charge-transfer (CT) states and are notable for determining the mechanism of free carrier generation and recombination processes.[8] The CT state energy (E_{CT}), defined as the energy required to promote the D–A complex from its ground state to its vibrationally relaxed first excited state, has been found to strongly depend on structural and conformational factors, such as the aggregation state of the donor and/or acceptor near the D/A junction, and the relative conformation of D and A molecules forming the CT complex.[9–14] Recent studies have revealed a strong dichroic absorption of CT complexes at planar interfaces in bilayers with crystalline donors, thus providing experimental evidence for oriented CT complexes.[15] Several models have related E_{CT} to the open-circuit voltage (V_{OC}) in organic solar cells.[2,16–18] The fundamental and striking feature that emerges from these models is that V_{OC} depends linearly on E_{CT} and only logarithmically on other factors such as the number, oscillator strength, and lifetime of the CT states.

Because of this linear dependence of V_{OC} on E_{CT}, strategies to improve V_{OC} are often oriented toward increasing E_{CT}. E_{CT} can be roughly viewed as the energy difference between the donor ionization potential (IP) and the acceptor electron affinity (EA), corrected to the binding energy between a hole in D molecule(s) and an electron on adjacent A molecule(s) within their respective environments, as highlighted schematically in **Figure 1**. Because the energy levels of both the donor and acceptor depend strongly on morphological factors such as

Dr. G. O. N. Ndjawa, Prof. K. R. Graham, Dr. B. D. Rose, Dr. S. Dey, Dr. L. Yu, Prof. J.-L. Brédas, Prof. A. Amassian
King Abdullah University of Science and Technology (KAUST)
Division of Physical Sciences & Engineering
and KAUST Solar Center (KSC)
Thuwal 23955-6900, Saudi Arabia
E-mail: aram.amassian@kaust.edu.sa

DOI: 10.1002/aenm.201601995

Prof. K. R. Graham, S. Mollinger, D. M. Wu, D. Hanifi, R. Prasanna, Prof. M. D. McGehee, Prof. A. Salleo
Department of Materials Science and Engineering
Stanford University
Stanford, CA 94305, USA
Prof. K. R. Graham
Department of Chemistry
University of Kentucky
Lexington, KY 40503, USA

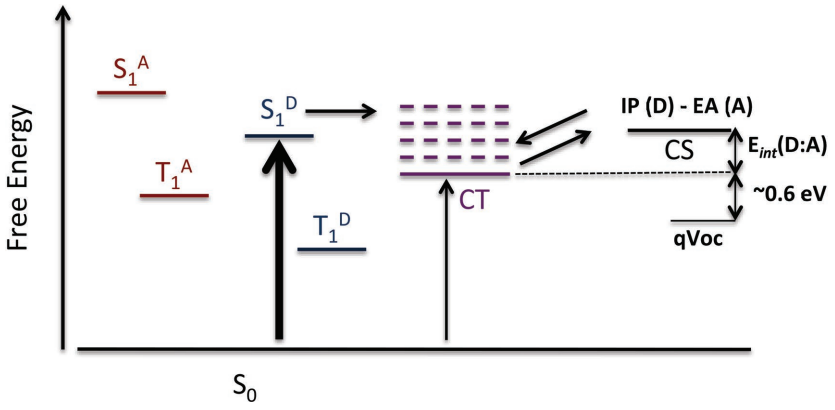

Figure 1. State diagram picture of an organic solar cell showing in solid lines the singlets and triplets states for a donor (D) and an acceptor (A), the charge-transfer (CT) state, and the charge-separated state (CS). Both singlet and CT states can be populated by direct optical excitation from the ground state S_0. IP(D) and IE(A) represent the ionization energy of the electron donor and the electron affinity of the electron acceptor while E_{int}(D: A)is the interaction/binding energy between the hole on the donor and the electron on the acceptor. Due to recombination losses, qV_{oc} is typically 0.6 eV lower than E_{CT}.[2,3,19]

crystallinity and molecular packing,[20–24] it is expected that in polymeric and small molecule organic materials there exists a relatively broad distribution of CT states. Recent studies have postulated equilibrium between free carrier generation and CT state formation near V_{OC} and established the dependence of V_{OC} on the chemical potential of the CT states.[2] The CT state chemical potential is determined by the statistical occupation of CT states, with lower lying CT states being exponentially more likely to be occupied. Therefore, the low energy CT states largely limit the V_{OC}. Hence, it is reasonable that a more successful approach to maximizing V_{OC} is to minimize or eliminate the presence of low energy CT states.

Factors that are expected to determine the distribution of CT states are donor or acceptor aggregation states, donor–acceptor separation and interfacial molecular conformations.[9,24,25] In their aggregated states, donor or acceptor domains typically have lower ionization potentials and increased electron affinities than the nonaggregated phases owing to polarization and delocalization effects.[25–27] Everything else remaining equal, nonaggregated (disordered) and aggregated (ordered) domains will thus form CT states of higher and lower energies, respectively.[15,28] The presence of such structural heterogeneities at the proximity of D–A interfaces will thus invariably influence the V_{OC}. Semicrystallinity is a staple of conjugated organic materials, in particular, in conjugated polymers where ordered and disordered regions typically coexist. Semicrystallinity can also be found in small molecule and oligomer systems, where crystallinity tends to be easier to control and noncrystalline regions can commonly be found.[29,30] Yet, to date there have been limited experimental studies systematically linking the influence of the inherent structural heterogeneities of organic semiconductors to the operation of organic solar cells, their V_{OC}, and the distribution of CT states at the D–A interface.

We take the view that model planar interfaces of D and A materials with well-controlled crystalline order should reveal how order and structural heterogeneities impact the CT state manifold and in turn increase or decrease the V_{OC}. In this study we use rubrene, a model donor small molecule, in combination with ultrahigh vacuum (UHV) deposition and controlled annealing to tune the microstructure, texture, and orientation of the donor as well as the degree of interfacial mixing with fullerene (C_{60}). In doing so, we isolate the impacts of donor order and orientation on the energy distribution of CT states in planar and bulk heterojunction systems. By annealing the amorphous rubrene films in different conditions, we attain films containing both amorphous and polycrystalline triclinic or orthorhombic phases. The same films are then used to evaluate E_{CT} and V_{OC} by making model bilayer solar cells without exposure to ambient air. We find that the E_{CT} present at the crystalline (c-) rubrene/C_{60} interface can be as much as ≈400 meV lower relative to E_{CT} at the amorphous (a-) rubrene/C_{60} interface. In cases where the donor contains both amorphous and crystalline phases, the CT manifold reflects these structural variations. By controllably introducing a discrete set of donor structures, we control the population of the CT states at the planar D–A interface and commensurately change the V_{OC} in a predictable fashion. The presence of low-lying CT states stemming from CT complexes formed between c-rubrene and C_{60} are shown to be responsible for V_{OC} loss by as much as 0.3 V in bilayer solar cells. By contrast, bilayer and bulk heterojunction solar cells containing only a-rubrene yield consistently high V_{OC} associated with the higher energy CT band.

2. Results and Discussions

2.1. Structural Order in Rubrene Thin Films and Its Influence on the Distribution of CT States

Rubrene (chemical structure shown in **Figure 2**a) is selected as the donor since it can be vacuum-sublimed into an amorphous thin film that can be subsequently crystallized through rapid thermal annealing without dewetting. The latter is an important requirement to fabricating working bilayer solar cells. Fullerene-C_{60} (C_{60}) is chosen as the acceptor (chemical structure shown in Figure 2a), as it is commonly used, is very similar to the widely used solution-processed [6,6]-phenyl C_{61} butyric acid methyl ester (PCBM), and has been shown to form rather abrupt interfaces with rubrene.[16] We have fabricated rubrene thin films with a wide range of structural order and textures. In addition to the crystalline phase formed, the extent of crystallinity of the rubrene film can be tuned by varying the duration of thermal annealing. Three types of rubrene samples, namely, amorphous rubrene (a-rubrene), triclinic rubrene (t-rubrene), and orthorhombic rubrene (o-rubrene) were fabricated. The a-rubrene was obtained as deposited. The t-rubrene was obtained by annealing the a-rubrene film at 150 °C for 120 s while the o-rubrene was obtained by annealing the a-rubrene at 170 °C for 300 s.

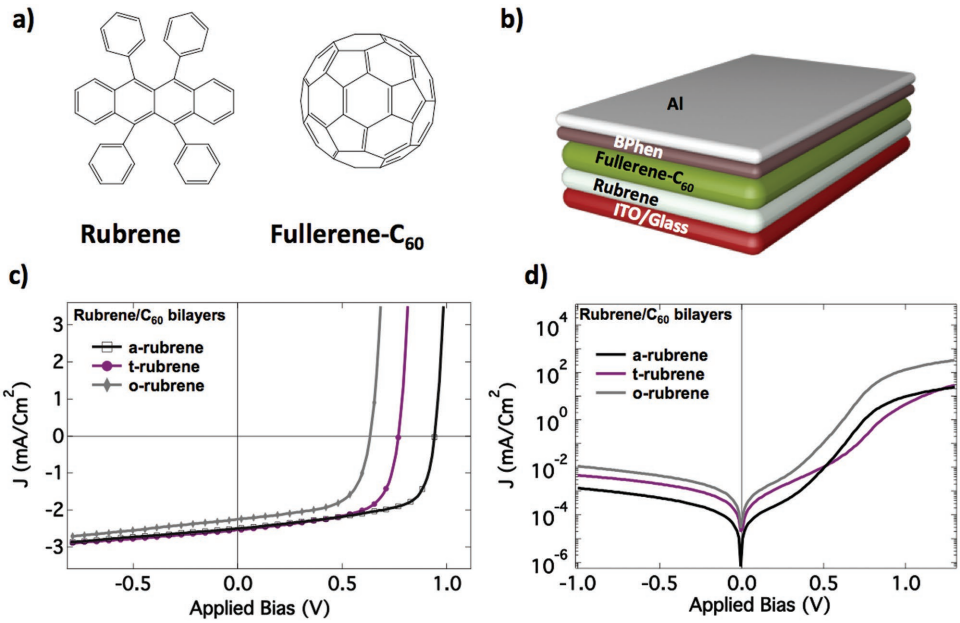

Figure 2. a) Chemical structures of rubrene and fullerene-C_{60}. b) Schematic illustration of the bilayer device structure. c) Illuminated and d) dark *J–V* characteristics of rubrene/C_{60} bilayer devices made with amorphous (a-rubrene) and partially crystallized rubrene films (t/o-rubrene).

We verify the structure of these rubrene films using grazing-incidence wide-angle x-ray scattering (GIWAXS). The scattering patterns for 50 nm thick films are shown in **Figure 3**. The as-deposited rubrene film exhibits no diffraction peak (Figure 3a), confirming its amorphous nature. The film annealed at 150 °C (Figure 3b) exhibits a diffraction pattern featuring two overlapping peaks, (100) and $(10\bar{1})$, in the out-of-plane direction (q_z direction) with a scattering vector amplitude of ≈0.870 Å^{-1} which is consistent with a triclinic phase of rubrene (P-1), lattice parameters of a = 7.01 Å, b = 8.54 Å, c = 11.95 Å, α = 97.5°, β = 104.7°, and γ = 98.8°.[31] The pattern also suggests that the film is textured with the oriented crystalline domains having their *a*-axis perpendicular to the substrate. In contrast, for the film annealed at 170 °C, the pattern appears to exhibit very sharp diffraction peaks in all crystallographic directions indicative of extended long range order in the film. The (002) diffraction peak with a q value of 0.474 Å^{-1} appearing in the out-of-plane direction shows that the highly oriented crystallites are formed in the orthorhombic phase (Cmca), with lattice parameters of a = 14.21 Å, b = 7.17 Å, and c = 26.78 Å, $\alpha = \beta = \gamma = 90°$,[31] with their *c*-axis oriented normal to the substrate. We also note the presence of relatively weak peaks associated with the triclinic rubrene phase in the film annealed at 170 °C (Figure 3c).

These results show that the rubrene films annealed at 150 or 170 °C exhibit differences in the crystalline phase (polymorphism) and the degree of order in agreement with other findings in the literature.[32,33] In addition, their surface termination differs markedly as indicated by their texture. In the absence of surface rearrangements, the film with the triclinic phase terminates with the tilted molecule with its aromatic core exposed (Figure 3e); whereas, for the film in the orthorhombic phase, the rubrene molecules are oriented side-on with only their phenyl rings exposed (Figure 3f). It is worth noting that other studies have found, through NEXFAS experiments, that the orientation of rubrene molecules at the surface of amorphous films is not completely random but instead exhibits a dominant conformation with the aromatic core exposed on average at the surface of the film (Figure 3d).[16,34] These differences in crystallinity, polymorphism, texture, and conformation are thus expected to translate into significantly different surface terminations with which the rubrene-C_{60} buried interface will form.

The successful fabrication of structurally distinct thin films of rubrene ranging from amorphous to polycrystalline with two different polymorphs and textures, has made it possible to investigate how the structural differences in the donor influence the operation of organic solar cells, their V_{OC} and the energetics of the D–A interface. We have fabricated bilayer solar cells using a-rubrene, t-rubrene, and o-rubrene as the donors, and C_{60} as the acceptor (glass/ITO-150 nm/rubrene-50 nm/C_{60}-50 nm/Bphen-12 nm/Al-100 nm, Figure 2b). As rubrene layers can exhibit pinholes and cracks upon annealing, which can impede device operation,[33,35] we deposited a partial monolayer (0.5 nm) of copper iodide (CuI) on ITO. The CuI layer, which has been shown to act as an effective seed layer for the growth of several organic donors,[36–38] had the benefit of maintaining the continuity of the rubrene films even after crystallization. In Figure 2c,d and **Table 1**, we summarize the current–voltage (*J–V*) characteristics and associated figures of merit of the rubrene/C_{60} bilayer devices. The open-circuit voltage (V_{OC}), as extracted from current–voltage characteristics of the bilayer devices (Table 1), drops substantially by 170 mV in going from the bilayer (BL) device with a-rubrene to that with t-rubrene. A further drop of 140 mV is observed in going from the device with t-rubrene to that with o-rubrene. The fill factor (FF) and the short-circuit current density (J_{sc}) vary marginally. The decrease in V_{OC} with annealing the donor is consistent with previous reports[35] using thicker films.

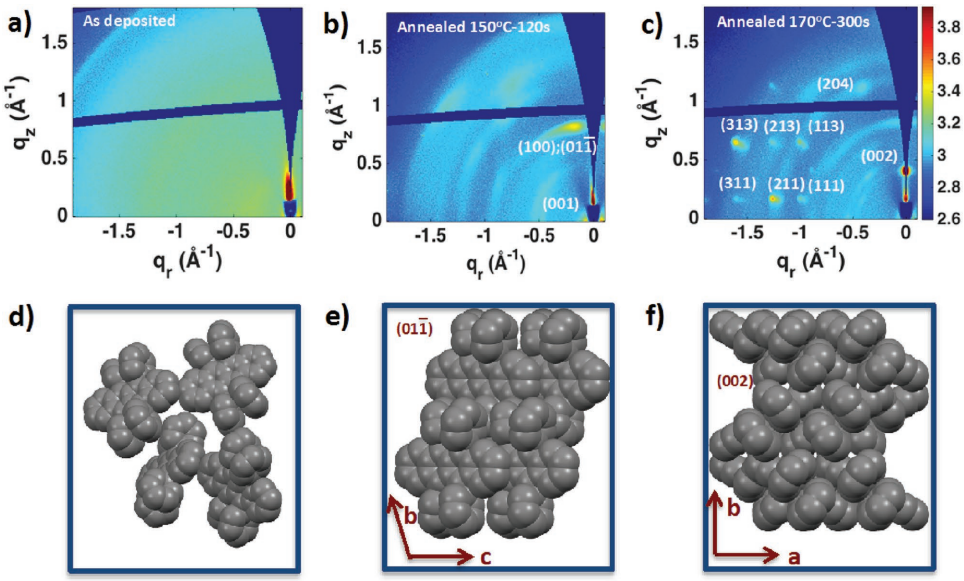

Figure 3. Top: 2D GIWAXS patterns of 50 nm thick rubrene films on ITO/glass substrates for a) the as-deposited a-rubrene film, b) t-rubrene film annealed at 150 °C for 120 s, and c) o-rubrene film annealed at 170 °C for 300 s. Bottom: Illustrations of the molecular structure near the surface of thin films of d) a-rubrene, e) t-rubrene, and f) o-rubrene. The molecular packing in a-rubrene films is shown to have an average orientation exposing the acene core of the molecules, in agreement with previous measurements.[34,39] The textured t-rubrene film exposes the (01 $\bar{1}$) plane of the triclinic system, placing the acene cores at the film surface. The textured o-rubrene film exposes the (002) plane, placing the side phenyl rings of rubrene at the surface while the acene core is less accessible.

As the bulk heterojunction (BHJ) solar cell represents the most common architecture of organic solar cells, we have also fabricated a BHJ device (glass/ITO-150 nm/rubrene-50 nm:C_{60}(1:1)-60 nm/C_{60}-10 nm/Bphen-12 nm/Al-100 nm) through codeposition of rubrene and C_{60} without additional annealing. As expected, the BHJ layer exhibits lower FF and Jsc than the BL devices (Table 1), as a result of lack of aggregation and phase separation in the blend, but it exhibits an identical V_{OC} to that of BL devices using a-rubrene. This strongly indicates that the a-rubrene/C_{60} interface in BL devices can successfully emulate the nature of the D–A interface in BHJ devices of the same materials. On the other hand, our efforts to anneal the BHJ layer to crystallize the rubrene phase have failed to yield working devices, preventing further direct comparisons between BL and BHJ devices at this time.

The significant drop in V_{OC} of BL devices exhibiting different structures of rubrene points to changes in energetics at the rubrene/C_{60} interface. V_{OC} is specifically related to the energy of the charge-transfer states, E_{CT}, at the D–A interface.[39–41] A very effective means of measuring the densities and the energies of charge-transfer states is to perform sensitive external quantum efficiency (EQE) measurements to detect the subgap photovoltaic response of the solar cells. These measurements rely on the excitation of interfacial CT complexes by direct optical transition with a spectrally resolved light source. Utilizing Marcus theory to model the absorbance of these D–A complexes, λ being the reorganization energy associated to the charge-transfer absorption process, and f the charge-transfer absorption cross-section scaled to the internal quantum efficiency of charge generation through direct CT state absorption, the subgap portion of the EQE spectrum of the device can be expressed by Equation (1)[41]

$$\mathrm{EQE}(E) = \frac{f}{E\sqrt{4\pi\lambda kT}} \exp\left(\frac{-\left(E_{CT}+\lambda-E\right)^2}{4\lambda kT}\right) \quad (1)$$

E_{CT}, λ, and f are obtained by fitting Equation (1) to the subgap region of the EQE spectrum.

Table 1. Annealing time, open-circuit voltage (V_{OC}), fill factor (FF), short-circuit current density (J_{sc}), integrated external quantum efficiency (EQE) signal, and power conversion efficiency (PCE) for rubrene/C_{60} BL and BHJ devices tested under 100 mW cm^{-2} simulated AM1.5 irradiation.

Description	a-rubrene (BL)	t-rubrene (BL)	o-rubrene (BL)	a-rubrene (BHJ)
Annealing time [s]	0	120	300	0
V_{OC} [V]	0.94 ± 0.03	0.77 ± 0.06	0.63 ± 0.02	0.92 ± 0.05
FF [%]	62.7 ± 0.3	62 ± 0.15	61.20 ± 0.05	22.7 ± 0.5
J_{sc} [mA cm^{-2}]	2.50 ± 0.03	2.54 ± 0.05	2.25 ± 0.03	1.050 ± 0.02
Integrated EQE signal [mA/cm^2]	2.55	2.50	2.10	0.95
PCE [%]	1.47 ± 0.02	1.21 ± 0.01	0.90 ± 0.03	0.2 ± 0.02

In **Figure 4**a,b, we show the measured EQE spectra of the rubrene/C_{60} BL and BHJ devices with corresponding fits, plotted on a logarithmic scale to highlight absorption features in the subgap region of the spectra (1 to 2 eV). The subgap absorption features are associated with interfacial CT states.[42] In the case of the BL and BHJ devices with an a-rubrene film, a single CT band is visible at 1.48 eV. As the rubrene film crystallizes, a clear and distinct CT band emerges at a spectral position lower in energy (1.23 eV for t-rubrene and 1.1 eV for o-rubrene) while the CT band at the spectral position of the purely amorphous case remains, decreasing in prominence. This indicates that annealing the rubrene films at 150 or 170 °C to produce the triclinic and orthorhombic phases, respectively, has the effect of modifying part of the D–A interface, making it energetically distinct from the starting interface with a-rubrene.

In Figure 4c, we show the values of E_{CT} extracted from the fits of the CT bands in the form of a bar graph. The spectral positions of all the CT bands in the spectra remain roughly invariant, with the CT bands associated to the t-rubrene/C_{60} and the o-rubrene/C_{60} interfaces appearing only in samples annealed at 150 and 170 °C, respectively. It is reasonable to attribute these low energy CT peaks to the t-rubrene/C_{60} and o-rubrene/C_{60} interfaces since a significant portion of the rubrene film surface is expected to be made of the ordered rubrene phases present in the bulk of the film (Figures S1 and S3, Supporting Information).[35,43] The presence of the prominent CT band at high energy indicates a substantial fraction of rubrene remains amorphous especially near the D–A interface. This interpretation is further supported by the decrease in the strength of the same CT bands with increased annealing time of the t-rubrene and o-rubrene layers (Figure S2, Supporting Information).

An independent approach to gain insight into the interfacial energy landscape is through electroluminescence (EL) measurements. EL has been used as a thermodynamic indicator of the available open-circuit voltage in organic solar cells.[42,44] The EL spectra of all rubrene/C_{60} bilayers were measured in order to independently determine the energy of the CT states. As shown in Figure 4d, for all devices, a CT state emission was detected in the near infrared region. For the device made with amorphous rubrene, the CT state emission appears at ≈1.32 eV. Upon annealing of the rubrene layer, we observe an invariable redshift of all CT emissions to ≈1.1 eV. In the devices with annealed rubrene, the amorphous rubrene phase present at the interface has no CT emission in part due to preferential population of the lower energy CT states. It has been observed in single crystal rubrene that although such low volume fraction amorphous inclusions play an important role in photophysical processes such as bulk photoluminescence, they have little influence on hole transport.[29] If we make the plausible assumption that holes are only transported through the low energy crystalline phase, their energy in this phase would thus determine where CT emission occurs at the interface. CT emission at ≈1.1 eV is therefore in agreement with EQE data and

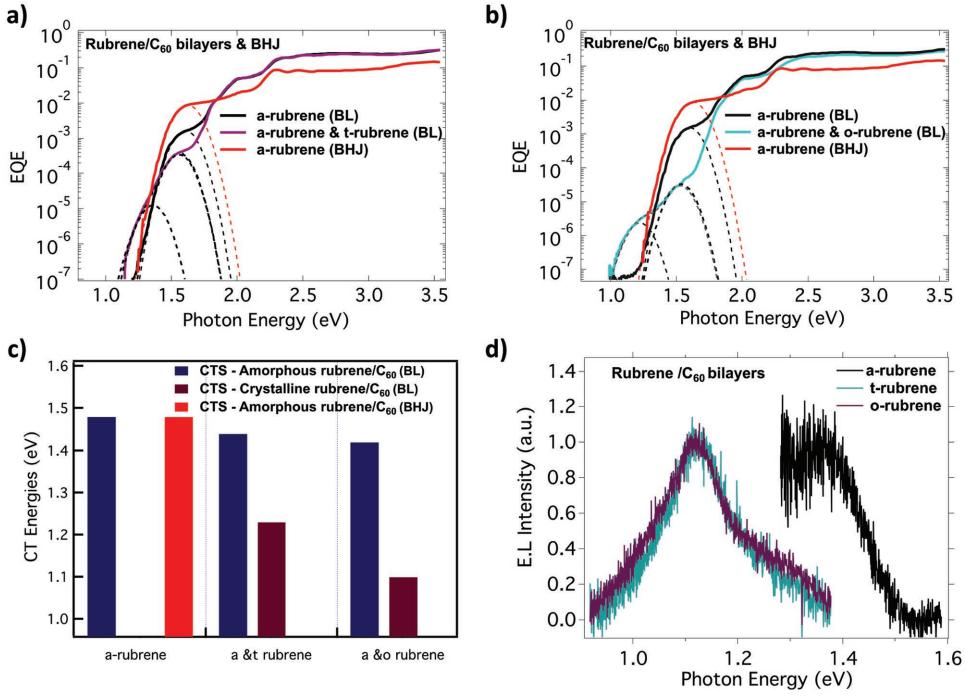

Figure 4. a,b) Subgap EQE spectra collected on bilayer devices fabricated with as-deposited and annealed rubrene layers. The spectra are shown on a logarithmic scale, to highlight the CT bands in the subgap region. In the case of as-deposited rubrene only a single CT band is visible. In the cases of annealed rubrene (t/o-rubrene), a second band clearly appears at significantly lower energy in addition to the CT band at high energy. The dotted lines indicate fits of Equation (1) to the CT bands. c) CT energies extracted from (a) and (b) for the high and low energy bands. d) Electroluminescence spectra of rubrene/C_{60} bilayers. The spectral position of the emission peak of the CT state of the devices with annealed rubrene appears to be independent of the annealing temperature of rubrene but red shifted by ≈0.22 eV with respect to the CT peak in the device with amorphous rubrene, confirming that predominantly low-lying CT states with energy 1.1 eV are present in the bilayers with annealed rubrene.

further substantiates the presence of low-lying CT states in the crystalline films.

2.2. First Principle Calculations to Understand the Origin of CT Energy Dependence on Interfacial Conformation of Rubrene

To gain more insight into why E_{CT} should vary depending on the structure of rubrene, we have performed density functional theory calculations following the methods described in the Experimental Section. As mentioned above, to a good approximation, E_{CT} can be expressed as in Equation (2)[45]

$$E_{CT} = IP_D - EA_A + E_{int}(D:A) \quad (2)$$

where IP_D is the ionization potential of the isolated donor phase, EA_A is the electron affinity of the isolated acceptor phase, and E_{int}(D: A) is the interaction energy that results when D and A are brought together to form an interface (Figure 1). Equation (2) suggests that variations in the donor ionization potential (IP_D) would induce variations in the E_{CT}. IP_D has been found to be strongly dependent on the degree of structural order and molecular orientation.[6,9,27,46–50] When C_{60} is used as the acceptor, the effect of acceptor orientation is minimal thanks to its spherical symmetry.

We have measured the IP of amorphous and crystalline rubrene layers by photoelectron spectroscopy (Figure S4, Supporting Information). We find that the IP of crystalline rubrene (t-rubrene and o-rubrene), independently of the annealing condition, decreases by ≈0.4 eV compared with a-rubrene. This drastic decrease in ionization potential with increased crystalline order will most likely play a role into lowering the CT state energy at the crystalline rubrene/C_{60} interface. However, as suggested by Equation (2), interactions owing to polarization and the relative orientation of the D and A molecules at the rubrene/C_{60} interface also factor into E_{CT}. In **Figure 5**, we show the calculated dependence of CT state energy on rubrene/C_{60} conformation. Face-on conformation results in CT states with the lowest energy while end-on and edge-on conformations result in slightly higher CT state energies. These calculations suggest that in the case of rubrene/C_{60}, out of the three main interfacial molecular conformations, two conformations result in high CT state energies. Based on this observation, we expect that in the case of a-rubrene, whereby rubrene molecules are randomly oriented, it will be more probable to encounter high-energy CT state conformations than the low energy conformation. However, a-rubrene films may have a preferential surface termination.[39] To test whether this might impact interfacial energetics, we have measured the CT state energy of the BHJ device described above and found it to be identical to that of the BL using a-rubrene (Figure 4a). This shows that surface texture effects are negligible in BL devices and confirms that the model BL system can well mimic the interfacial properties of the BHJ, as previously indicated by comparing the V_{OC} of BL and BHJ devices.

While the absolute values of the calculated E_{CT} are expected to be somewhat different from the experimentally determined values, their relative shifts should carry meaning. The fact that for all the three conformations assessed in the calculations

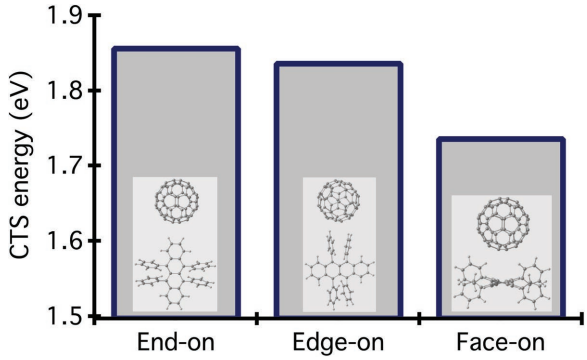

Figure 5. Whether the D and A molecules touch end-on, edge-on, or face-on would influence the energy of the CT state. In a bilayer configuration with amorphous rubrene, the rubrene molecules are expected to be isotropically distributed and to present a homogeneous interface that would form in the presence of C_{60} a distribution of CT states that is centered around a certain mean value. Edge-on, side-on, and face-on conformations correspond to CT energies of 1.86, 1.84, and 1.74 eV, respectively, meaning a decrease of 0.1 eV between face-on, edge-on, and side-on conformations.

carried out on complexes made of a single rubrene and a single C_{60} molecule, the maximal CT energy shifts by only ≈100 meV, compared with an experimental shift of 380 meV, points to other factors contributing to lowering the CT energy at the crystalline rubrene/C_{60} interface. As discussed above, the annealed rubrene films are textured differently and exhibit different crystalline structures (Figure 3 and Figure S1, Supporting Information). The resulting surface terminations (Figure 3e,f) lead to two very different molecular conformations of the donor, yet the corresponding E_{CT} (1.23 eV vs 1.1 eV) differs by only ≈130 meV, in agreement with the simplified theoretical calculations. Comparing with the case of a-rubrene for which the disordered film surface exhibits a preferential molecular conformation and gives rise to the highest E_{CT} (1.48 eV), points to the potential importance of packing order within the donor film. Thus, the question arises whether the extent of aggregation and crystalline order of the donor can be playing a much more important role than conformational differences at the D–A interface.

It is well known that crystalline rubrene can exhibit band-like transport, which is a manifestation of the high degree of electronic delocalization. Likewise, previous theoretical work[9] on tetracene/C_{60} bilayers show that face-on conformation and tetracene packing, through delocalization effects, lower the E_{CT}. Furthermore, the low ionization potential of the annealed rubrene films is indicative that the hole is more stabilized in the crystalline phase, i.e., effectively more delocalized. In situ ultraviolet photoelectron spectroscopy (UPS) measurements performed at different stages of C_{60} deposition on amorphous and crystalline phases of rubrene indicate there is little or no intermixing, therefore resulting in a nominally abrupt D/A interface in BL systems (Figure S5, Supporting Information).[39] Thus, it can be reasonably concluded that crystalline rubrene/C_{60} interfaces will form predominantly low energy CT states and that hole delocalization[51] within the aggregated rubrene phase will in fact account for most of the measured 0.38 eV difference in E_{CT} between a-rubrene/C_{60} and t-,o-rubrene/C_{60} interfaces.

2.3. Roles of Triplet Excitons Dynamics at Interfaces Containing Both Amorphous and Crystalline Rubrene Phases

Triplet recombination and energy transfer processes may be partly responsible for the difference in $E_{CT} - qVoc$ observed between a- and o-rubrene. Several groups have elucidated exciton dynamics at the rubrene/C_{60} interface and it was found that triplet–triplet annihilation contributes significantly to photocurrent in the amorphous device, while this process reduces photocurrent in the crystalline device.[52–54] Photoluminescence studies have also shown that triplet fusion is more efficient in a-rubrene than in crystalline rubrene, and the existence of triplet transfer from the crystalline phase to the amorphous phase.[29] If these recombination and energy transfer processes lead to increased nonradiative recombination at the interfaces with crystalline rubrene, it becomes difficult to assign V_{OC} loss solely to the presence of low energy CT states. We compare the difference $E_{CT} - qV_{OC}$ for bilayers in which rubrene is the most disordered (a-rubrene/C_{60}) and exhibits the most order (o-rubrene/C_{60}; annealed for 300 s). In the latter case, we make the provisional assumption that the lowest CT energy determines the V_{OC}. As we found that $E_{CT} - qV_{OC}$ only differs by 70 meV (540 vs 470 meV) for the amorphous and annealed cases, respectively, we do not expect differences in the amount of nonradiative recombination to influence the difference in V_{OC} significantly. Similarly, J_{sc} and FF are comparable for all devices. Thus, it is possible that there are intricate photophysical processes involving rubrene triplet states that enable the apparent current losses at the crystalline rubrene/C_{60} interface to be recycled. These processes may also impact the CT band strengths at the amorphous rubrene/C_{60} and crystalline rubrene/C_{60} interfaces in devices with annealed rubrene. However, other factors such as differences in the number of charge-transfer state complexes should also be considered as we discuss in the Supporting Information.

2.4. Estimating the V_{OC} in the Presence of Multiple Interfacial CT Bands

To evaluate the relative influence of the two CT bands on V_{OC}, we have used a recently developed model[2] that expresses V_{OC} exclusively in terms of CT states characteristics. According to this model, V_{OC} is equated to the chemical potential of CT states. As such, it is expressed in term of the energy of the CT state, its population and its lifetime. One of the attractive features of the model is that it is easily generalizable to systems exhibiting more than one CT band. Considering contributions from CT states at the interfaces with both amorphous and crystalline rubrene, and that at V_{OC} the recombination current density (J_{rec}) is equal to J_{sc}, the photocurrent density generated by the device can be expressed as in Equation (3)[2]

$$J_{sc} = J_{rec} = \frac{qN_{ct}}{\tau_{ct}} = \frac{q}{\tau_{ct}}\left(\underbrace{N_{oa}\, e^{\frac{qV_{oc}-E_{cta}}{kT}}}_{\text{amorphous}} + \underbrace{N_{oc}\, e^{\frac{qV_{oc}-E_{ctc}}{kT}}}_{\text{crystalline}}\right) \quad (3)$$

Here, N_{oa} and N_{oc} are the total numbers of interfacial CT states formed at the interface between C_{60} and the amorphous and crystalline phases of rubrene, respectively; τ_{ct} is the CT state lifetime and E_{cta} and E_{ctc} are the CT state energies associated to the amorphous and crystalline (triclinic or orthorhombic) phases and J_{rec} is the recombination current at V_{OC}. We make the simplifying assumption that the CT lifetime, τ_{ct}, is identical for the CT states at all three interface types. Solving Equation (3) for V_{OC} we arrive at Equation (4), which allows us to calculate the V_{OC} based on the data extracted from EQE measurements and using a value for τ_{ct} comparable to literature values.[55]

$$V_{oc} = -\frac{kT}{q}\ln\left(\frac{q}{\tau_{ct} * J_{sc}}\right) - \frac{kT}{q}\ln\left(\underbrace{N_{oa}\, e^{\frac{-E_{cta}}{kT}}}_{\text{amorphous}} + \underbrace{N_{oc}\, e^{\frac{-E_{ctc}}{kT}}}_{\text{crystalline}}\right) \quad (4)$$

In **Figure 6**, we compare the predicted and experimental V_{OC} values for all bilayer devices assuming a single lifetime of $\tau_{ct} = 5$ ns. The reason for this choice and other assumptions we have made in our calculations are discussed in detail in the Supporting Information. While the quantitative agreement appears to be good, we caution that this is subject to change if a different value of τ_{ct} were selected (see Supporting Information for additional comparisons based on $0.5 < \tau_{ct} < 10$ ns). However, importantly, we find the predicted V_{OC} perfectly tracks the trend in the experimental V_{OC}, which further emphasizes that V_{OC} very much reflects the composition of the CT manifold and underlines the significant role of low-lying CT states in pinning the V_{OC}. Such low-lying CT states are due to the presence of ordered donor and/or acceptor domains at the D/A interface.

In the case of BHJ solar cells where interfacial structural order is conceivably much harder to realize, and for which interfacial area is significantly larger, we expect a much larger number of interfacial molecular configurations to become accessible and the interfacial energetic landscape to be characterized by a much broader distribution of CT states.[56] The findings of this work suggest that the relative number of the

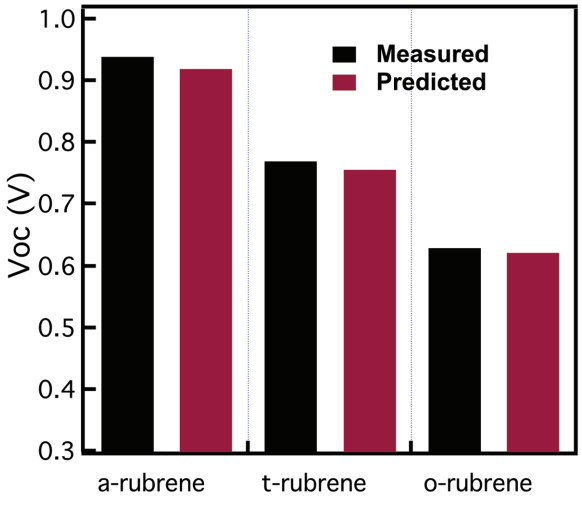

Figure 6. Experimental and predicted values of V_{OC} for rubrene/fullerene-C_{60} bilayer solar cells using Equation (4) along with quantitative analysis of the CT state manifold.

lowest lying CT states is orders of magnitude smaller but that their low energy has a dramatic effect on V_{OC}.

3. Conclusions

In this work, we have shown that the coexistence of ordered and disordered phases and polymorphs exhibiting different CT energetics constitute important limiting factors for the V_{OC} in organic solar cells. In the rubrene-C_{60} system, the rubrene phase that is ordered enables the formation of charge-transfer states that are as much as 380 meV lower in energy than CT states formed by the disordered phase. The presence of such energetically low-lying CT states primarily controls the amount of voltage that the cell can produce. For the rubrene-C_{60} system, the presence of such states with low E_{CT} translates into V_{OC} loss amounting to up to 310 meV in rubrene-C_{60} devices made with partially ordered rubrene. Our results underline once again the compromise that has to be reached in terms of formation of delocalized states, which favor charge separation but lower E_{CT} and increase nonradiative recombination to the ground state.[25,51]

Considering BHJ devices for which the interfacial area is substantially greater and where the development of structural order of the donor and acceptor phases can be easily inhibited, the coexistence of different phases poses an important challenge to maximizing the V_{OC}. Yet, semicrystallinity and polymorphism are staples of conjugated materials commonly used in organic photovoltaics. Semicrystallinity of certain conjugated polymers, such as P3HT, stems from the permanent coexistence of ordered and disordered phases.[57,58] In order to prevent V_{OC} loss it is therefore crucial to realize interfacial structural control that results in high CT states and eliminates the presence of low-lying CT states. This requires that the design of new conjugated donors and acceptors incorporates the need for realizing interfaces with locally disordered donor and acceptor so as to maximize the CT state energy, while nearby donor and acceptor domains are kept pure and exhibit the required degree of aggregation and crystallinity to assure sufficiently rapid charge transport and minimize the opportunity for charge recombination. In this respect, the existence of a thin interfacial mixed phase throughout the BHJ would be crucial. Such systems would be based on donors that can spontaneously mix with acceptors.[27,59]

4. Experimental Section

Materials: Copper iodide and fullerene-C_{60} (sublimed grade) were purchased from Sigma-Aldrich. Rubrene (triple sublimed) was purchased from Jilin OLED Materials. All materials were used as purchased without further purification.

Ultraviolet Photoelectron Spectroscopy: The rubrene films used for UPS analysis were deposited on gold-coated mica substrates in an Omicron ultra-high vacuum (UHV) molecular beam epitaxy (MBE) chamber at KAUST, and transferred without breaking vacuum to the adjacent analysis chamber for characterization. The base pressure of 1×10^{-10} mbar in both chambers. The rubrene films were deposited at ≈0.8 Å s^{-1} with the substrate held at room temperature. Thermal annealing was performed in the UHV MBE chamber when required. When probing intermixing, the fullerene-C_{60} overlayer was deposited in a stepwise manner. UPS of the films was measured with He (I) excitation (21.22 eV). The Omicron SPHERA hemispherical electron energy analyzer was used to generate the spectra with pass energies of 3.0 eV. The lamp intensity was attenuated to minimize the photodegradation of the rubrene film. The analyzer resolution (105 meV) was determined by measuring the width of the Fermi edge of a sputtered cleaned polycrystalline gold foil. The ionization potential of the film was determined by adding to the film work function, the valence band onset.

Subgap EQE: The EQE spectra were taken at short-circuit condition under focused monochromatic illumination from xenon arc. The light beam was modulated by an optical chopper (275 Hz). The device output current was measured as a function of photon energy using a lock-in amplifier (Stanford Instruments SR 830). The lamp intensity was calibrated with Ge and Si photodiodes.

Device Fabrication: The patterned ITO-coated glass substrates were sequentially cleaned with soap, water, acetone, and isopropanol in an ultrasonic bath for 15 min for each step followed by a 12 min UV-ozone exposure. All the layers films were deposited in an Angstrom evaporation chamber system with a base pressure of 10^{-7} mbar on top of precleaned ITO substrates at rates of 0.01 Å s^{-1} (CuI), 0.8 Å s^{-1} (rubrene), 1 Å s^{-1} (C_{60}), 0.5 Å s^{-1} (BPhen), and 1 Å s^{-1} for aluminum.

Device Characterization: The current–voltage characteristics of the bilayer solar cells were recorded in the nitrogen glove box under AM1.5 simulated illumination (ABET technology) with a spectral irradiance of 100 mW cm^{-2}. The lamp intensity was calibrated using a reference silicon photodiode.

Grazing Incidence Wide-Angle X-ray Scattering: GIWAXS measurements were performed at D-line at the Cornell High Energy Synchrotron Source (CHESS) and at the Advanced Light Source (ALS). At CHESS, a 0.5 mm × 0.1 mm monochromatic X-ray beam (double-bounce multilayer monochromator) with 1.15 Å wavelength was used. The diffractograms were recorder using a 50 × 50 mm2 charged coupling device (CCD) area detector (Medoptics) with pixel size of 172 µm. Experiments were performed at a grazing incidence angle of 0.15° with respect to the substrate plane. The detector was placed at a distance of 149 mm from the sample stage.

Atomic Force Microscopy (AFM): The surface morphology of rubrene films was examined using tapping mode AFM (Agilent 5400).

Scanning Tunneling Microscopy (STM): STM imaging was performed in a variable temperature STM (VT-STM; Omicron Nanotechnology) operated in UHV conditions (5.0×10^{-10} mbar). The samples were kept at room temperature during measurements. For imaging, chemically etched polycrystalline tungsten STM tip was used, which was further cleaned by electron bombardment in situ in UHV to reach the atomically resolved structure of HOPG. STM images were acquired with the applied sample bias of $V_b = 0.8$ V and a tunneling current of $I_t = 0.5$ nA.

UV–Vis Absorption: Absorption spectra were acquired with a Cary 5000 (Varian) spectrophotometer equipped with an integrating sphere on rubrene/C60 bilayer films prepared on quartz substrates in the same conditions used for device fabrication.

Photothermal Deflection Spectroscopy (PDS): PDS spectra were collected at Stanford University, Salleo Group, using a home-built apparatus. The bilayer samples were excited by illumination with monochromatic light from a 150 W Xenon lamp chopped at 3.333 Hz. The deflection of the probe beam (HeNe laser, 633 nm) in perfluorohexane was detected by a position-sensitive Si detector. The PDS signal was extracted from the detector signal using a Stanford Research Systems lock-in amplifier (Stanford Instruments SR 830). The PDS spectra were set to absolute scale by matching the UV–Vis spectra collected with the integrating sphere.

Electroluminescence (EL): EL spectra were measured on bilayers solar cells without air exposure. The emitted light was detected with a cooled InGaAs CCD array detector. Bias was applied using a Keithley 236 source measurement unit.

Computational Methods: The geometries of rubrene and C_{60} were independently optimized using the ωB97X-D functional[60] with the 6–31G(d,p) basis set. The combined rubrene and C_{60} molecules were then placed in the canonical orientations considered and a rigid scan

was performed to yield three low-energy structures (Figure 4). The charge-transfer states were calculated at the LC-BLYP/6-311G(d,p) level; the range-separation parameter ω for the LC-BLYP functional[61] was optimized by the ionization potential tuning procedure[62] for isolated rubrene and C_{60} and then using the averaged ω-value ($\omega = 0.191$ bohr^{-1}) and the maximum overlap method;[63] polarization effects were accounted for through the C-PCM model.[64,65] All calculations were performed with the 2014 GAMESS program package.[66]

Supporting Information

Supporting Information is available from the Wiley Online Library or from the author.

Acknowledgements

The Office of Competitive Research Funds at the King Abdullah University of Science and Technology supported this work in part under the CRG-3 program (A.A. and J.-L.B.). J.-L.B. acknowledges support in part from the Office of Naval Research–Global under Award No. N62909-15-1-2003. This work was also supported in part by the ONR Award Nos. N00014-14-1-0580 and N00014-16-1-2520. Portions of this work were done at the Cornell High Energy Synchrotron Source (CHESS). G.O.N.N., K.R.G., M.D.M., and A.A. acknowledge the Office of Competitive Research Funds for a GRP-CF award. K.R.G. and A.A. acknowledge SABIC for a postdoctoral fellowship. A.A. acknowledges SABIC for the Career Development SABIC Chair. The authors thank Dr. Detlef-M. Smilgies for help with acquisition of GIWAXS data at CHESS. CHESS was supported by the NSF & NIH/NIGMS via NSF Award No. DMR-1332208. The authors also acknowledge Dr. Sean Ryno for helpful discussions. Figure 3 was updated on January 17, 2017 to remove a formatting error. The scientific content was not changed.

Received: September 7, 2016
Revised: November 18, 2016
Published online: January 16, 2017

[1] K. Vandewal, J. Widmer, T. Heumueller, C. J. Brabec, M. D. McGehee, K. Leo, M. Riede, A. Salleo, *Adv. Mater.* **2014**, *26*, 3839.
[2] T. M. Burke, S. Sweetnam, K. Vandewal, M. D. McGehee, *Adv. Energy Mater.* **2015**, *5*, 1.
[3] R. A. J. Janssen, J. Nelson, *Adv. Mater.* **2013**, *25*, 1847.
[4] T. Krichartz, K. Taretto, U. Rau, *J. Phys. Chem. C* **2009**, *1*, 17958.
[5] S. R. Forrest, *MRS Bull.* **2005**, *30*, 28.
[6] S. Sweetnam, K. R. Graham, G. O. Ngongang Ndjawa, T. Heumuller, J. A. Bartelt, T. M. Burke, W. Li, W. You, A. Amassian, M. D. McGehee, *J. Am. Chem. Soc.* **2014**, *136*, 14078.
[7] T. M. Burke, M. D. McGehee, *Adv. Mater.* **2014**, *26*, 1923.
[8] J.-L. Brédas, J. E. Norton, J. Cornil, V. Coropceanu, *Acc. Chem. Res.* **2009**, *42*, 1691.
[9] B. Yang, Y. Yi, C. Zhang, S. G. Aziz, V. Coropceanu, J.-L. Brédas, *J. Phys. Chem. C* **2014**, *118*, 27648.
[10] B. Bernardo, D. Cheyns, B. Verreet, R. D. Schaller, B. P. Rand, N. C. Giebink, *Nat. Commun.* **2014**, *5*, 3245.
[11] M. Olguin, R. R. Zope, T. Baruah, *J. Chem. Phys.* **2013**, *138*, 74306.
[12] M. Schubert, B. A. Collins, H. Mangold, I. A. Howard, W. Schindler, K. Vandewal, S. Roland, J. Behrends, F. Kraffert, R. Steyrleuthner, Z. Chen, K. Fostiropoulos, R. Bittl, A. Salleo, A. Facchetti, F. Laquai, H. W. Ade, D. Neher, *Adv. Funct. Mater.* **2014**, *24*, 4068.
[13] A. Zusan, K. Vandewal, B. Allendorf, N. H. Hansen, J. Pflaum, A. Salleo, V. Dyakonov, C. Deibel, *Adv. Energy Mater.* **2014**, *4*, 1.
[14] C. R. Zhang, J. S. Sears, B. Yang, S. G. Aziz, V. Coropceanu, J. L. Brédas, *J. Chem. Theory Comput.* **2014**, *10*, 2379.
[15] A. N. Brigeman, M. A. Fusella, Y. Yan, G. E. Purdum, Y.-L. Loo, B. P. Rand, N. C. Giebink, *Adv. Energy Mater.* **2016**, *6*, 1601001.
[16] K. R. Graham, P. Erwin, D. Nordlund, K. Vandewal, R. Li, G. O. Ngongang Ndjawa, E. T. Hoke, A. Salleo, M. E. Thompson, M. D. McGehee, A. Amassian, *Adv. Mater.* **2013**, *25*, 6076.
[17] K. Vandewal, K. Tvingstedt, A. Gadisa, O. Inganäs, J. V Manca, *Nat. Mater.* **2009**, *8*, 904.
[18] K. Vandewal, K. Tvingstedt, J. V Manca, O. Inganäs, *IEEE J. Sel. Top. Quantum Electron.* **2010**, *16*, 1676.
[19] J.-L. Brédas, J. E. Norton, J. Cornil, V. Coropceanu, *Acc. Chem. Res.* **2009**, *42*, 1691.
[20] M. Bö, T. Schemme, D. H. De Jong, C. Denz, A. Heuer, N. L. Doltsinis, *Phys. Chem. Chem. Phys.* **2015**, *17*, 28616.
[21] P. Brown, D. Thomas, A. Köhler, J. Wilson, J.-S. Kim, C. Ramsdale, H. Sirringhaus, R. Friend, *Phys. Rev. B* **2003**, *67*, 1.
[22] Y. Zhong, S. Izawa, K. Hashimoto, K. Tajima, T. Koganezawa, H. Yoshida, *J. Phys. Chem. C* **2015**, *119*, 23.
[23] N. Koch, *Phys. Status Solidi RRL* **2012**, *6*, 277.
[24] T. W. Holcombe, J. E. Norton, J. Rivnay, C. H. Woo, L. Goris, C. Piliego, G. Gri, O. A. Sellinger, J. Br, A. Salleo, J. M. J. Fréchet, *J. Am. Chem. Soc.* **2011**, *133*, 12106.
[25] B. Yang, Y. Yi, C.-R. Zhang, S. G. Aziz, V. Coropceanu, J.-L. Brédas, *J. Phys. Chem. C* **2014**, *118*, 27648.
[26] N. Sato, K. Seki, H. Inokuchi, *J. Chem. Soc., Faraday Trans. 2* **1981**, *77*, 1621.
[27] K. R. Graham, G. O. N. Ndjawa, S. M. Conron, R. Munir, K. Vandewal, J. J. Chen, S. Sweetnam, M. E. Thompson, A. Salleo, M. D. Mcgehee, A. Amassian, *Adv. Energy Mater.* **2016**, *6*, 1601211.
[28] Y. L. Lin, M. A. Fusella, O. V. Kozlov, X. Lin, A. Kahn, M. S. Pshenichnikov, B. P. Rand, *Adv. Funct. Mater.* **2016**, *26*, 6489.
[29] Y. Chen, B. Lee, D. Fu, V. Podzorov, *Adv. Mater.* **2011**, *23*, 5370.
[30] J. A. Love, C. M. Proctor, J. Liu, C. J. Takacs, A. Sharenko, T. S. Van Der Poll, A. J. Heeger, G. C. Bazan, T. Q. Nguyen, *Adv. Funct. Mater.* **2013**, *23*, 5019.
[31] S. Obata, T. Miura, Y. Shimoi, *Jpn. J. Appl. Phys.* **2014**, *53*, 7.
[32] P. S. Jo, D. T. Duong, J. Park, R. Sinclair, A. Salleo, *Chem. Mater.* **2015**, *27*, 3979.
[33] H. M. Lee, H. Moon, H. S. Kim, Y. N. Kim, S. M. Choi, S. Yoo, S. O. Cho, *Org. Electron.* **2011**, *12*, 1446.
[34] C. H. Wang, A. K. M. M. Islam, Y. W. Yang, T. Y. Wu, J. W. Lue, C. H. Hsu, S. Sinha, M. Mukherjee, *Langmuir* **2013**, *29*, 3957.
[35] B. Verreet, P. Heremans, A. Stesmans, B. P. Rand, *Adv. Mater.* **2013**, *25*, 5504.
[36] L. A. Rochford, A. J. Ramadan, D. S. Keeble, M. P. Ryan, S. Heutz, T. S. Jones, *Adv. Mater. Interfaces* **2015**, *2*, 2.
[37] G. O. Ngongang Ndjawa, K. R. Graham, R. Li, S. M. Conron, P. Erwin, K. W. Chou, G. F. Burkhard, K. Zhao, E. T. Hoke, M. E. Thompson, M. D. McGehee, A. Amassian, *Chem. Mater.* **2015**, *27*, 5597.
[38] K. Zhao, G. O. Ngongang Ndjawa, L. K. Jagadamma, A. El Labban, H. Hu, Q. Wang, R. Li, M. Abdelsamie, P. M. Beaujuge, A. Amassian, *Nano Energy* **2015**, *16*, 458.
[39] K. R. Graham, P. Erwin, D. Nordlund, K. Vandewal, R. Li, G. O. Ngongang Ndjawa, E. T. Hoke, A. Salleo, M. E. Thompson, M. D. McGehee, A. Amassian, *Adv. Mater.* **2013**, *25*, 6076.
[40] K. Vandewal, A. Gadisa, W. D. Oosterbaan, S. Bertho, F. Banishoeib, I. Van Severen, L. Lutsen, T. J. Cleij, D. Vanderzande, J. V. Manca, *Adv. Funct. Mater.* **2008**, *18*, 2064.
[41] K. Vandewal, K. Tvingstedt, A. Gadisa, O. Inganäs, J. V. Manca, *Phys. Rev. B* **2010**, *81*, 125204.
[42] K. Tvingstedt, K. Vandewal, A. Gadisa, F. Zhang, J. Manca, O. Inganäs, *J. Am. Chem. Soc.* **2009**, *131*, 11819.

[43] H. M. Lee, H. Moon, H. S. Kim, Y. N. Kim, S. M. Choi, S. Yoo, S. O. Cho, *Org. Electron.* **2011**, *12*, 1446.
[44] U. Rau, *Phys. Rev. B* **2007**, *76*, 85303.
[45] S. M. Ryno, M. K. Ravva, X. Chen, H. Li, J.-L. Brédas, *Adv. Energy Mater.* **2016**, 1601370.
[46] S. Sweetnam, R. Prasanna, T. M. Burke, J. A. Bartelt, M. D. McGehee, *J. Phys. Chem. C* **2016**, *120*, 6427.
[47] W. Chen, S. Chen, H. Huang, D. C. Qi, X. Y. Gao, A. T. S. Wee, *Appl. Phys. Lett.* **2008**, *92*, 63308.
[48] L. Zhang, S. S. Roy, R. J. Hamers, M. S. Arnold, T. L. Andrew, *J. Phys. Chem. C* **2015**, *119*, 45.
[49] Y. Yi, V. Coropceanu, J.-L. Brédas, *J. Am. Chem. Soc.* **2009**, *131*, 15777.
[50] W. Chen, D. C. Qi, Y. L. Huang, H. Huang, Y. Z. Wang, S. Chen, X. Y. Gao, A. T. S. Wee, *J. Phys. Chem. C* **2009**, *113*, 12832.
[51] X.-K. Chen, M. K. Ravva, H. Li, S. M. Ryno, J.-L. Brédas, *Adv. Energy Mater.* **2016**, *6*, 1601325.
[52] A. Ryasnyanskiy, I. Biaggio, *Phys. Rev. B*, **2011**, *84*, 2.
[53] H. Mattoussi, H. Murata, C. D. Merritt, Z. H. Kafafi, *Proc. SPIE* **1998**, December, 49.
[54] A. K. Pandey, *Sci. Rep.* **2015**, *5*, 7787.
[55] T. M. Burke, S. Sweetnam, K. Vandewal, M. D. McGehee, *Adv. Energy Mater.* **2015**, *5*, 1500123.
[56] D. B. Sulas, K. Yao, J. J. Intemann, S. T. Williams, C. Z. Li, C. C. Chueh, J. J. Richards, Y. Xi, L. D. Pozzo, C. W. Schlenker, A. K. Y. Jen, D. S. Ginger, *Chem. Mater.* **2015**, *27*, 6583.
[57] P. Pingel, A. Zen, R. D. Abellón, F. C. Grozema, L. D. A. Siebbeles, D. Neher, *Adv. Funct. Mater.* **2010**, *20*, 2286.
[58] J. Zhao, Y. Li, A. Hunt, J. Zhang, H. Yao, Z. Li, J. Zhang, F. Huang, H. Ade, H. Yan, *Adv. Mater.* **2016**, *28*, 1868.
[59] J. J. Chen, S. M. Conron, P. Erwin, M. Dimitriou, K. McAlahney, M. E. Thompson, *ACS Appl. Mater. Interfaces* **2015**, *7*, 662.
[60] J.-D. Chai, M. Head-Gordon, *Phys. Chem. Chem. Phys.* **2008**, *10*, 6615.
[61] Y. Tawada, T. Tsuneda, S. Yanagisawa, T. Yanai, K. Hirao, *J. Chem. Phys.* **2004**, *120*, 8425.
[62] T. Koerzdoerfer, J. L. Brédas, *Acc. Chem. Res.* **2014**, *47*, 3284.
[63] A. T. B. Gilbert, N. A. Besley, P. M. W. Gill, *J. Phys. Chem. A* **2008**, *112*, 13164.
[64] V. Barone, M. Cossi, *J. Phys. Chem. A* **1998**, *102*, 1995.
[65] O. L. Griffith, J. E. Anthony, A. G. Jones, D. L. Lichtenberger, *J. Am. Chem. Soc.* **2010**, *132*, 580.
[66] M. W. Schmidt, K. K. Baldridge, J. A. Boatz, S. T. Elbert, M. S. Gordon, J. H. Jensen, S. Koseki, N. Matsunaga, K. A. Nguyen, S. Su, T. L. Windus, M. Dupuis, J. A. Montgomery, *J. Comput. Chem.* **1993**, *14*, 1347.